

Why Do Stars Turn Red?

PO-SHENG OU (歐柏昇) ^{1,2} AND KE-JUNG CHEN (陳科榮) ¹

¹*Institute of Astronomy and Astrophysics, Academia Sinica, No.1, Sec. 4, Roosevelt Rd., Taipei 10617, Taiwan, R.O.C.*

²*Department of Physics, National Taiwan University, No.1, Sec. 4, Roosevelt Rd., Taipei 10617, Taiwan, R.O.C.*

ABSTRACT

When a star exhausts the hydrogen fuel in its core, the core contracts, and the envelope may expand to ~ 100 times its original size. Consequently, stars with $\lesssim 8$ solar masses become red giants, while those with $\gtrsim 8$ solar masses evolve into red supergiants. However, the physics driving this extreme expansion is unclear. This letter presents a new mechanism grounded in the instability of stellar envelopes to explain the expansion. If the gravitational energy released by core contraction can trigger the initial expansion to a critical radius where the envelope becomes unstable, the star then continues expanding until stabilizing, thereby becoming a red giant or supergiant. We demonstrate that the envelope instability can explain several elusive features in the Hertzsprung–Russell diagram, such as the Hertzsprung gap between the main sequence and the red giant branch, as well as the dichotomy of the supergiant populations in red and blue.

Keywords: Stellar physics (1621) — Stellar evolution (1599) — Red giant stars (1372) — Red supergiant stars (1375)

1. INTRODUCTION

The existence of red giants (RGs) and red supergiants (RSGs) as a theoretical solution in stellar astrophysics is well established; however, the question of why stars turn red, becoming RG/RSGs, remains in debate. Classical theories often refer to the “mirror effect”, which describes reciprocal motion resulting from the release of gravitational energy as the helium core contracts (Maeder 2009; Kippenhahn et al. 2013). While the “mirror effect” provides an explanation to the expansion of post-main-sequence stars, it does not fully explain why stars transition to certain radii with a red color.

Various theories have been proposed to explain why a star becomes an RG/RSG, attributing the key role to factors such as degree of core contraction (Eggleton & Cannon 1991; Faulkner 2005), thermal imbalance driven by opacity (Renzini et al. 1992; Renzini & Ritossa 1994; Ritossa 1996; Renzini 2023), gradients of the opacity and mean molecular weight (Sugimoto & Fujimoto 2000), and the pressure and density contrast between the shell and the core (Miller Bertolami 2022). Some other authors suggested that no single factor plays a major role (Whitworth 1989; Iben 1993). Despite these varied theories, there has been no consensus on what precisely drives stars to turn red.

The observed distribution of giants and supergiants on the Hertzsprung–Russell (HR) diagram presents intriguing puzzles. A notable observed phenomenon is the “Hertzsprung gap” (Hoyle 1960), a region with very low stellar density that bridges the main sequence and the red giant branch (RGB). This gap is conventionally attributed to the rapid evolution of stars towards the RGB. However, the precise reason why stars rapidly pass through this region, instead of lingering, remains elusive. Another notable phenomena is division of supergiants into two distinct categories: RSGs and blue supergiants (BSGs). The scarcity of yellow supergiants (Drout et al. 2009; Neugent et al. 2012; Yang et al. 2019, 2021), which would exhibit intermediate effective temperatures (T_{eff}), results in a gap between BSGs and RSGs. To explain the dichotomy between RSGs and BSGs would require a deeper understanding of stellar physics.

A clue to understanding the physics of stellar evolution into RG/RSG is the concept of “critical metallicity” required for RSG formation, as suggested by recent stellar models (Ou et al. 2023). According to these models, not all stars successfully evolve into RSGs during their core-helium (He) burning phase. Only stars with metallicities above a specific threshold can transition

into RSGs; those below this threshold remain as BSGs with smaller radii. Thus, the stable state of a supergiant can be either red or blue, typically not yellow. The transition between these two phases is characterized by a discontinuous change in radii and T_{eff} across different metallicities. This discontinuous transition between the RSG and BSG phases should be governed by a specific physical criterion.

2. METHODS

To investigate the physical origin of RSGs, we construct stellar models using the Modules for Experiments in Stellar Astrophysics (MESA; Paxton et al. 2011, 2013, 2015, 2018, 2019; Jermyn et al. 2023) No.10108. MESA is a one-dimensional stellar evolution code that includes microphysics such as nuclear reaction networks, equations of state, and opacities.

We develop stellar models with initial masses of $3-60M_{\odot}$. For stars with masses of $\leq 10M_{\odot}$, we employ settings from the test suite “1M_pre_ms_to_wd” to evolve the stars from pre-main-sequence stage to the white dwarf phase. For stars with masses of $\geq 11M_{\odot}$, we first calculate pre-main-sequence evolution to create zero-age-main-sequence (ZAMS) models, then continue to evolve these models from the ZAMS to iron core collapse. We adopt the default settings for massive stars from the “inlist_massive_defaults” file within the `MESASTAR` module for simulations after the ZAMS.

3. ENERGY SOURCES FOR EXPANSION

First, we compare two models of stars, each with an initial mass of $25M_{\odot}$; one with an absolute metallicity $Z = 5 \times 10^{-3}$ and the other with $Z = 5 \times 10^{-4}$. This comparison is shown in Figure 1 (details about the rate of heat flow are described in Appendix A). The star with higher metallicity successfully evolves into an RSG, whereas the star with lower metallicity only reaches the BSG stage during its core-He burning phase. Despite of different metallicities, the heat released from core contraction into the envelope is comparable for both models. The higher metallicity star that evolves into an RSG does not receive more energy from its core for envelope expansion. Therefore, the “mirror effect” alone is insufficient to explain the formation of RSGs.

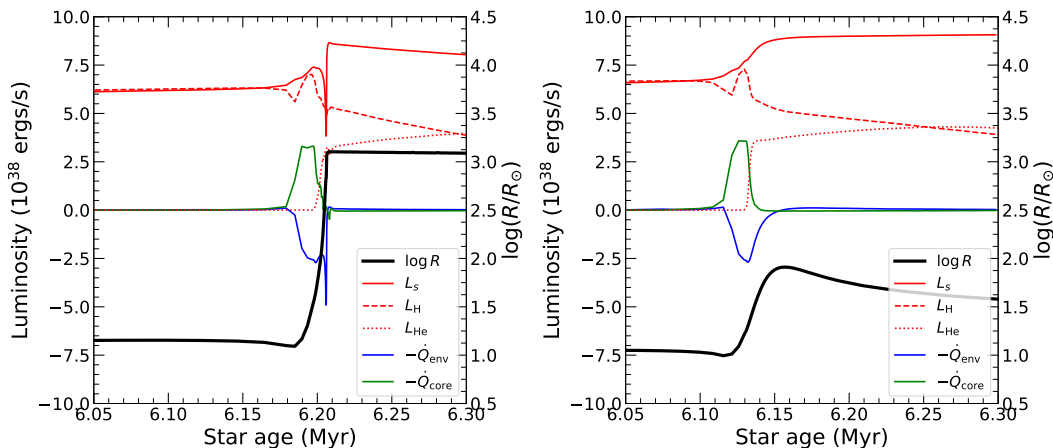


Figure 1. Evolution of various energy generation rates for a $25M_{\odot}$ star with different metallicities during the expansion. The high-metallicity ($Z = 5 \times 10^{-3}$) model that eventually evolves into an RSG (*left panel*) and the low-metallicity ($Z = 5 \times 10^{-4}$) model that only evolves into a BSG (*right panel*) are compared. The stellar radii (R), the surface luminosities (L_s), the energy generation rate by shell-H burning (L_H), the energy generation rate by core-He burning (L_{He}), and the \dot{Q} term, which is the rate of heat flow, for the stellar envelope (\dot{Q}_{env}) and for the stellar core (\dot{Q}_{core}) are plotted.

Following core contraction, stellar nuclear reactions mainly take place in the hydrogen (H) shell and He core. As shown in Figure 1, it is not the difference in the energy generation from these nuclear reactions that drive the RSG formation. The energy generation rate by either shell-H burning or core-He burning is not significantly higher in the stars that eventually become RSGs. Instead, these stars expand into RSGs by trapping more energy within their envelopes, at the expense of their surface luminosities. A sharp decrease in surface luminosity is a distinctive characteristic in the transition to an RSG, a feature that is absent in stars that evolve only into BSGs. It is this luminosity drop, rather than an increase in energy generation, that provides the energy required for the envelope to expand into an RSG.

A straightforward explanation for this luminosity drop could be that increased opacity within the stellar envelope traps more energy from outgoing radiation, thereby driving the expansion towards the RSG phase. However, as shown in Figure 2, the stellar

models progressing to RSGs do not always exhibit higher opacities. In fact, even models with significantly reduced opacities can still reach the RSG extent as long as the nuclear reaction rates are high enough. This indicates that factors beyond simple opacity variations are responsible for RSG formation.

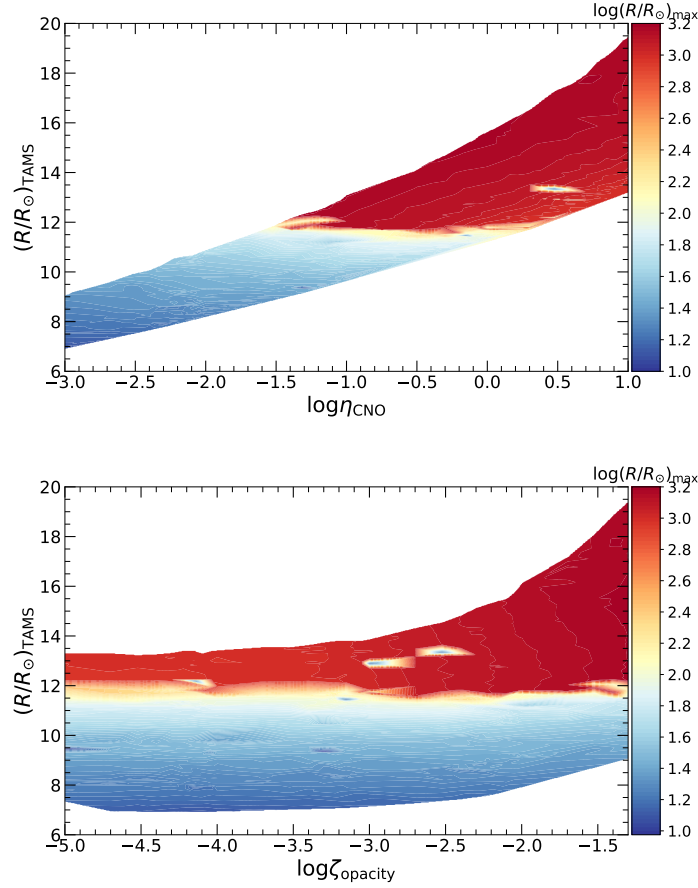


Figure 2. Relationship among pre-expanded radii, hydrogen burning rates, envelope opacities, and final maximum radii. The TAMS radii (R_{TAMS}) and the maximum radii during the core-He burning phase (R_{max}) of stars with an initial mass of $25 M_{\odot}$ and metallicity of $Z = 0.001$ but different CNO reaction rates and opacities are shown. The R_{TAMS} of each model is displayed using a color representing its R_{max} . The same dataset is displayed along CNO reaction rates (*top panel*) and opacities (*bottom panel*), respectively. η_{CNO} represents a linear scaling factor of the original CNO rates. ζ_{opacity} represents the input metallicity to retrieve opacity from the opacity tables. The higher ζ_{opacity} typically yields higher opacity. From these diagrams, most of the stars with R_{TAMS} larger than the threshold at $\sim 12 R_{\odot}$ eventually become RSGs.

4. ENVELOPE INSTABILITY

4.1. Stellar radius and envelope instability

Our study suggests that the determining factor for a star’s evolution into an RSG is its size prior to expansion, which is the product of evolution with various stellar parameters such as opacity and nuclear reaction rates during the main-sequence stage. To evolve into an RSG, a star must achieve a threshold size at the end of the main-sequence stage, known as the terminal-age main sequence (TAMS). Figure 2 demonstrates this concept with various stellar models, all with the initial mass of $25 M_{\odot}$ but exhibiting different radii at the TAMS. The details of these models are described in Appendix B. For these $25 M_{\odot}$ stars, only those with radii larger than ~ 12 solar radii (R_{\odot}) at the TAMS successfully become RSGs, while the others remain as BSGs. This threshold radius for RSG formation varies with different stellar masses.

Only stars that surpass a certain radius threshold at the TAMS can eventually become RSGs. We suggest that this is largely due to a radius range of *envelope instability*, as depicted in Figure 3, which shows how surface pressure changes with a growing radius in the post-main-sequence stage. As the radius expands, the surface pressure of the star first decreases, then increases,

and finally decreases again. A decrease in surface pressure with an expanding radius indicates stability, as the star naturally reverts to its initial radius after a small perturbation. In contrast, in a region where the surface pressure increases as the radius expands, even a small perturbation in radius can lead to further expansion, indicating instability. For $25 M_{\odot}$ stars, there exists an unstable radius range at $\sim 200\text{--}600 R_{\odot}$, with small variations influenced by metallicity. This instability due to the change in surface pressure as a function of radius is similar to the instabilities involved in the derivation of the Jeans length (Jeans 1902) and the Schönberg–Chandrasekhar limit (Schönberg & Chandrasekhar 1942).

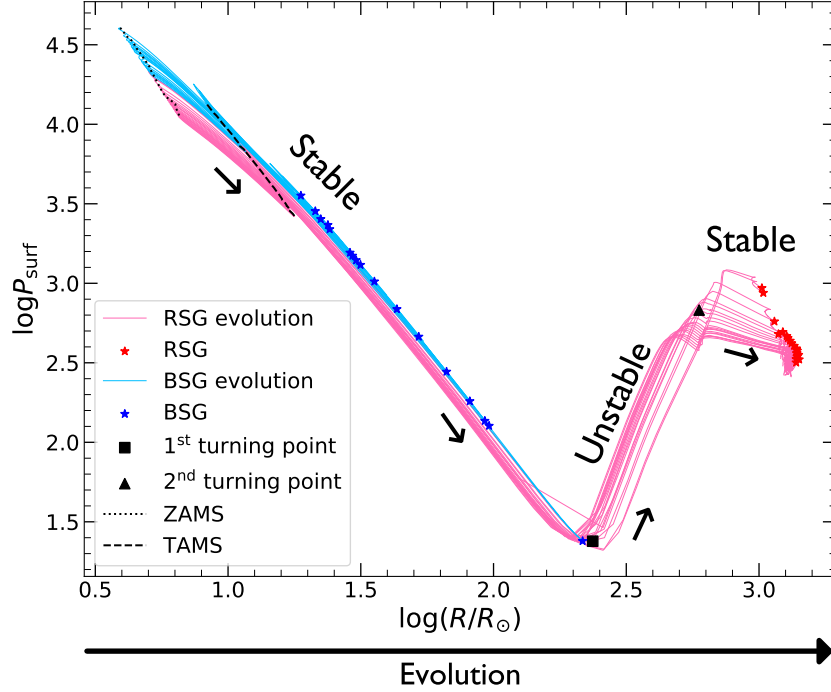


Figure 3. Evolution of surface pressure (P_{surf}) versus radius. Each curve represents an evolutionary track of a $25 M_{\odot}$ star with different metallicities. The metallicities are $Z = (1, 2, \dots, 9) \times 10^{-5}$, $(1, 2, \dots, 9) \times 10^{-4}$, $(1, 2, \dots, 9) \times 10^{-3}$, and $(1.0, 1.1, 1.2, \dots, 2.0) \times 10^{-2}$. The evolutionary tracks of stars leading to RSGs are colored in red, while those of stars becoming BSGs are in blue. The red and blue star icons mark the location of R_{max} for RSGs and BSGs, respectively. Notably, none of the star icons is located within unstable radius range. We mark the two turning points of slope changes on the curve of $Z = 0.007$ with a square and a triangle, respectively, to demonstrate the boundaries of the instability zone as presented in Figure 4 and Figure 5. The timings of the ZAMS and the TAMS are also marked on the evolutionary tracks.

We suggest that the formation of RSGs is driven by the envelope instability. In Figure 3, the star icons represent the maximum radii that stars reach during their core-He burning stage. Notably, no star remains within the unstable radius range, leading to a clear division into two distinct groups: RSGs and BSGs. For the stars with smaller TAMS radii due to factors such as low metallicity, the “mirror effect” leads to expansion only within the first stable radius range, so these stars remain as BSGs. In contrast, stars that are sufficiently large at the TAMS are expanded into the unstable radius range by the “mirror effect”. Once the stars enter this unstable range, they cannot maintain their size but continue expanding until their radii reach the next stable zone. This continued expansion in the instability zone is what causes them to turn red. This mechanism explains why the RSG phase is distinctly separate from BSGs in stellar evolution.

4.2. Formation of blue and red supergiants

The evolution of supergiants encompasses two distinct stages, each caused by different physical mechanisms: the transformation from the main sequence to BSGs, followed by the expansion from BSGs to RSGs. Generally, all massive stars are capable of expanding into BSGs through the “mirror effect”. However, advancing beyond this stage, from BSG to RSG, requires more than just the “mirror effect”. The key determinant for this second stage of expansion is the presence of envelope instability. Only if the star is large enough at the TAMS, larger than $\sim 12 R_{\odot}$ for $25 M_{\odot}$ stars, the “mirror effect” can expand the star into the unstable

radius range, causing further expansion into the RSG phase. Conversely, the $25M_{\odot}$ stars with radii at the TAMS smaller than $\sim 12R_{\odot}$ only expand into the BSG phase and do not further transition into the RSG phase.

The energy source for the expansion from the main sequence to BSGs is simply the gravitational energy released by He-core contraction. The further expansion from BSGs to RSGs is triggered by envelope instability, rather than by any additional energy source. Therefore, this expansion requires a sacrifice of the surface luminosity, leading to a sharp luminosity drop, as shown in Figure 1.

4.3. Envelope instability criteria for 3 to $60M_{\odot}$ stars

The existence of envelope instability is not exclusive to massive stars such as those with $25M_{\odot}$; it is generally applicable for stars of 3 to $60M_{\odot}$. In Figure 4, we show the relationship between T_{eff} and stellar radii for stars within this mass range. The envelope instability zone is delineated by identifying the two turning points on the curve of surface pressure versus radius for each star, similar to the curves in Figure 3. These turning points define the lower and upper limits of the unstable radius range of each star. This range varies continuously with stellar mass, with lower-mass stars exhibiting instability at smaller radii. As a result, the radii after expansion are smaller for lower-mass stars compared to more massive stars. Nevertheless, T_{eff} at these limits, ~ 8000 K for the lower limits and ~ 4500 K for the upper limits, are roughly consistent across different stellar masses, as shown in the boundary of the instability zone of Figure 4.

Our results suggest that the formation of RGs with initial masses larger than $\sim 3M_{\odot}$ and RSGs originate from the same physical mechanism of envelope instability. However, for RGs with initial masses less than $\sim 2M_{\odot}$, we cannot identify instability zones or corresponding luminosity drops during their expansion phases. The formation of these RGs is probably associated with helium flashes rather than envelope instability, and therefore, they are beyond the scope of this study.

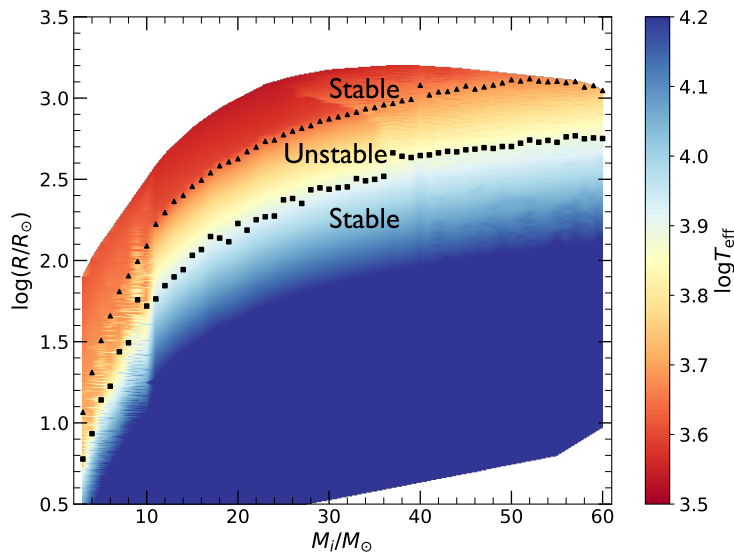


Figure 4. Radius range and the corresponding effective temperatures of the envelope instability zone across stellar masses. The envelope instability zones for $3-60M_{\odot}$ stars with $Z = 0.007$ (Large Magellanic Cloud metallicity) are shown. The instability zones are delineated by the turning points of slope changes on the surface pressure versus radius curves, as demonstrated in Figure 3. The lower limits of the instability zones are marked by squares, and the upper limits are marked by triangles. Colors represent the T_{eff} of the stars of given initial masses when they evolve to certain radii. The upper boundary of the red region represents R_{max} , the maximum radii of RGs and RSGs at the core-He burning stage.

5. THE ORIGIN OF HERTZSPRUNG GAP ON THE HR DIAGRAM

The envelope instability can explain some notable observational phenomena on the HR diagram. In Figure 5, we have converted the luminosities and T_{eff} of theoretical stellar evolutionary tracks into observable magnitudes and color indices using the bolometric correction tables from the MESA Isochrones and Stellar Tracks (MIST) project (Dotter 2016; Choi et al. 2016). This conversion allows us to directly map the envelope instability zone along with the observed stellar population in the Large Magellanic Cloud (LMC) on the HR diagram. Since our stellar models cover a wide range of stellar masses, we separately compare

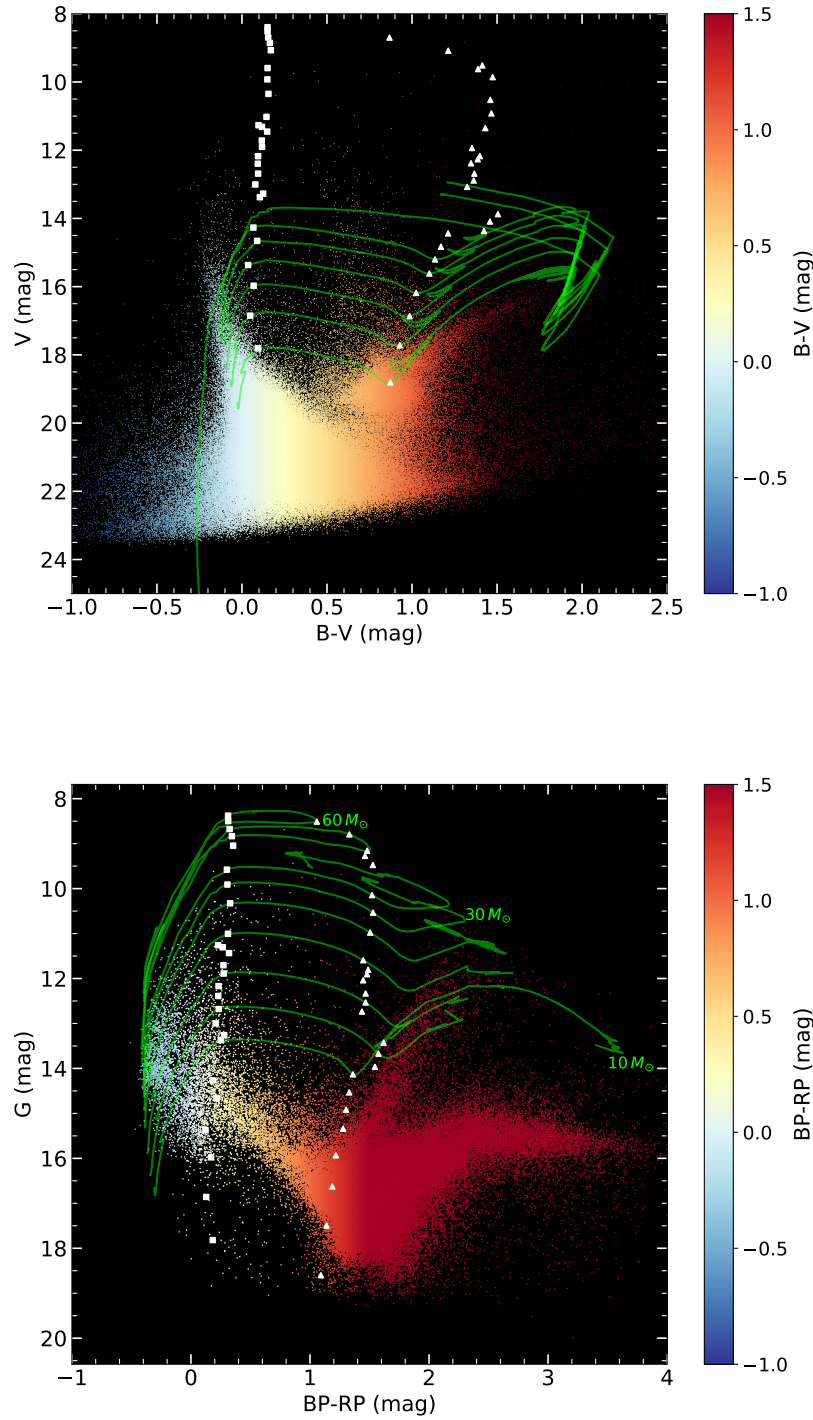


Figure 5. Color-magnitude diagrams of LMC stars overlaid with stellar evolutionary tracks marked with their envelope instability zones. The top panel is a color-magnitude diagram for a circular region with a 0.5 degree radius in the northwest arm of the LMC, mainly showing lower-mass stars (less than $\sim 8M_{\odot}$). The bottom panel displays a color-magnitude diagram of bright stars in the entire LMC, showing evolved massive stars. In both panels, the boundaries of the envelope instability zone for each stellar model are marked with a white square and a white triangle, respectively. The evolutionary tracks of the stellar models are shown with green lines. The stellar models are with the LMC metallicity ($Z = 0.007$) and different initial masses. For boundaries of the envelope instability zones (white markers) in both panels, the initial masses are 3, 4, 5, ..., 19, 20, 25, 30, ..., $60M_{\odot}$, from below upward. The evolutionary tracks on the top panel are with initial masses of 3, 4, 5, 6, 7, and $8M_{\odot}$, and those on the bottom panel are with initial masses of 10, 12, 15, 20, 25, 30, 35, 50, and $60M_{\odot}$.

the instability zones for RGs from 3 to $8M_{\odot}$ stars with the Magellanic Clouds Photometric Survey (MCPS; Zaritsky et al. 2004) data, and for RSGs from 10 to $60M_{\odot}$ stars with Gaia Data Release 2 (Gaia Collaboration 2018; Yang et al. 2021). The details of the method for these color-magnitude diagrams are described in Appendix C.

For our investigation of RGs, we selected a circular region with a radius of 0.5 degrees in the northwest arm of the LMC. We obtained the B and V band magnitudes of stars in this region from the MCPS. The color-magnitude diagram of these stars, presented in the top panel of Figure 5, shows the main sequence, the RGB, and the Hertzsprung gap between them. Notably, the envelope instability zone that we have identified matches well with the Hertzsprung gap. This result supports the existence of envelope instability zone and explains the physical origin behind the Hertzsprung gap between the main sequence and the RGB; because the limited number of stars within the Hertzsprung gap can be explained by the instability zone, which leads to a short transit phase of $\sim 10^5$ years that stars swiftly evolve through.

For evolved massive stars, we compare the theoretical instability zone with the Gaia data of the LMC bright stars, using the catalog compiled by ref. (Yang et al. 2021). In the color-magnitude diagram shown in the bottom panel of Figure 5, these stars are distributed into one group of RSGs and another group of BSGs, separated by a sporadic distribution of YSGs between them. The population counts for each type of evolved stars are as follows: 2974 RSGs, 508 YSGs, and 4786 BSGs (Yang et al. 2021). By overlaying the envelope instability zone on this color-magnitude diagram, we observe that this zone matches well with the sporadic distribution of YSGs. This result suggests that the instability zone clearly separate the populations between RSGs and BSGs in the color-magnitude diagram. We infer that supergiants predominantly appear as either blue or red because these colors correspond to stable zones, where stars stay for most of their time. In contrast, the YSGs are relatively rare because they are located within the instability zone. Massive stars rapidly evolve from BSGs to RSGs, passing through the YSG phase in a short period of $\sim 10^4$ years.

Furthermore, it is intriguing to note that the envelope instability zone coincides with the well-known instability strip in the HR diagram. For example, many observed YSGs are variable stars (Arellano Ferro 1981; Schmidt 1984; Dorn-Wallenstein et al. 2020). This overlap suggests a possible link between the envelope instability and the mechanisms driving stellar pulsation, which remains an area for further research.

6. CONCLUSIONS

In conclusion, we suggest that the instability of stellar envelope is key for a star to turn red. As the moderate expansion caused by the ‘‘mirror effect’’ propels a star into the unstable radius range, it naturally continues expanding until it reaches a stable radius, thus becoming an RG/RSG. The envelope instability zone on the HR diagram provides a self-consistent description of the observed Hertzsprung gap and the bifurcation of supergiants into red and blue categories.

This research is supported by the National Science and Technology Council, Taiwan under grant number MOST 110-2112-M-001-068-MY3 and by the Academia Sinica, Taiwan under the career development award AS-CDA-111-M04. Our simulations were performed at the National Energy Research Scientific Computing Center (NERSC), a U.S. Department of Energy Office of Science User Facility operated under Contract No. DE-AC02-05CH11231, and on the TIARA Cluster at the Academia Sinica Institute of Astronomy and Astrophysics (ASIAA).

Software: MESA (Paxton et al. 2011, 2013, 2015, 2018, 2019; Jermyn et al. 2023)

APPENDIX

A. CALCULATION OF THE RATE OF HEAT FLOW

From the MESA output, we obtain the ϵ_{grav} term, which is the negative value of rate of heat flow per unit mass, expressed as

$$\epsilon_{\text{grav}} \equiv -T \frac{\partial s}{\partial t}, \quad (\text{A1})$$

where T is the temperature, s is the specific entropy, and t is the time. The ϵ_{grav} term is usually used to diagnose stellar expansion (when $\epsilon_{\text{grav}} < 0$) and contraction (when $\epsilon_{\text{grav}} > 0$). To quantify the overall change in heat, we integrate the ϵ_{grav} term across either the core or the envelope:

$$-\dot{Q} \equiv \int_{M_1}^{M_2} \epsilon_{\text{grav}} dm, \quad (\text{A2})$$

where m is the mass coordinates, and M_1 and M_2 define the lower and upper limits of the mass range for calculation. Note that the physical meaning of ϵ_{grav} is the negative rate of heat flow per unit mass, rather than directly representing the rate of gravitational energy release (Paxton et al. 2011; Kippenhahn et al. 2013).

B. MODELS OF VARIOUS OPACITIES AND NUCLEAR REACTION RATES

As shown in Figure 2, we investigate how R_{TAMS} influence supergiant size by developing a grid of MESA models for $25 M_{\odot}$ and $Z = 0.001$ stars with various opacities and CNO cycle rates. The details of these models are as follows.

The opacity in our models is adjusted by using different ζ_{opacity} , referred to as Z_{base} in the MESA code, which is the input metallicity value used in the opacity table, not necessarily identical to the stellar metallicity used for evolution. For example, if we set $\zeta_{\text{opacity}} = 0.02$ for a star with $Z = 0.001$, its opacity used for the radiation transport calculation is equivalent to a star of $Z = 0.02$, but its metallicity for stellar evolution remains $Z = 0.001$. The adjustment of ζ_{opacity} is intended only to examine the opacity effect on envelope expansion, instead of producing realistic stellar models. Generally, a higher ζ_{opacity} results in increased opacity.

The reaction rates of the CNO cycle are changed by applying a linear scaling factor η_{CNO} . We change the rates for the five main reactions of the CNO cycle:

- (1) $^{12}\text{C} + ^1\text{H} \rightarrow ^{13}\text{N} + \gamma$,
- (2) $^{14}\text{N} + ^1\text{H} \rightarrow ^{15}\text{O} + \gamma$,
- (3) $^{16}\text{O} + ^1\text{H} \rightarrow ^{17}\text{F} + \gamma$,
- (4) $^{15}\text{N} + ^1\text{H} \rightarrow ^{16}\text{O} + \gamma$, and
- (5) $^{15}\text{O} + ^1\text{H} \rightarrow ^{12}\text{C} + ^4\text{He}$.

Changing the CNO reaction rates is for experiments on stellar evolution, rather than to construct realistic models.

From each models in this grid, which varies in opacity and nuclear reaction rates, we calculate the two radii: (1) R_{TAMS} and (2) the maximum radius during the core-He burning stage (R_{max}), representing the supergiant size. The relationship between R_{TAMS} and R_{max} is shown in Figure 2, which highlights the threshold radius required for RSG formation.

C. METHOD FOR THE COLOR-MAGNITUDE DIAGRAMS

We select the LMC, a nearby galaxy with low extinction, as a laboratory to compare observations with the theoretical envelope instability zone. We use two different observational dataset to create color-magnitude diagrams: one for massive stars (ranging from $\sim 10-60 M_{\odot}$) and another for lower-mass stars (ranging from $\sim 3-8 M_{\odot}$).

For the study of lower-mass stars, we use the Johnson B and V magnitudes of LMC stars from the Magellanic Clouds Photometric Survey (MCPS; Zaritsky et al. 2004). This survey was conducted using the Las Campanas Swope Telescope (1 m) and the Great Circle Camera, covering the central 8.5 by 7.5 degrees of the LMC. We select a circular region with a radius of 0.5 degrees centered at RA=05:00:00, Dec=-66:00:00, located in the northwest arm of the LMC. We extract the MCPS data for stars within this region to create a color-magnitude diagram using the B magnitudes and B-V color indices.

To investigate massive evolved stars, we utilize the multiwavelength catalog of bright sources in the LMC compiled by Yang et al. (2021). This catalog contains 197,004 sources and was constructed by crossmatching and deblending between the source list of Spitzer Enhanced Imaging Product and Gaia Data Release 2 (Gaia Collaboration 2018). Gaia astrometry is used to remove the foreground contamination, ensuring that the data specifically represents LMC stars. From this catalog, we extract the Gaia G band magnitude and Gaia BP-RP color to create a color-magnitude diagram.

To compare the theoretical stellar evolutionary tracks with observational data, we use the bolometric correction values to convert luminosities to magnitudes, and T_{eff} to color indices for the stellar models of the LMC metallicity ($Z = 0.007$). The bolometric correction tables are from the MESA Isochrones and Stellar Tracks (MIST) project (Dotter 2016; Choi et al. 2016). We apply these bolometric corrections for each timestep of a theoretical evolutionary track through tri-linear interpolation of the values in the tables based on T_{eff} , gravitational acceleration $\log g$, and the LMC's average extinction value $A_V = 0.3$ (Imara & Blitz 2007). The theoretical quantities are converted into Johnson B, Johnson V, Gaia G, Gaia BP, and Gaia RP band magnitudes. The distance modulus of 18.5 is applied to transform the absolute magnitudes to apparent magnitudes for LMC objects. These conversion allows us to overlay the evolutionary tracks and the boundaries of instability zones on color-magnitude diagrams. In Figure 5, we mark the instability zones calculated from stellar models with the LMC metallicity on the color-magnitude diagrams.

REFERENCES

- Arellano Ferro, A. 1981, PASP, 93, 351, doi: [10.1086/130837](https://doi.org/10.1086/130837)
- Choi, J., Dotter, A., Conroy, C., et al. 2016, ApJ, 823, 102, doi: [10.3847/0004-637X/823/2/102](https://doi.org/10.3847/0004-637X/823/2/102)

- Dorn-Wallenstein, T. Z., Levesque, E. M., Neugent, K. F., et al. 2020, *ApJ*, 902, 24, doi: [10.3847/1538-4357/abb318](https://doi.org/10.3847/1538-4357/abb318)
- Dotter, A. 2016, *ApJS*, 222, 8, doi: [10.3847/0067-0049/222/1/8](https://doi.org/10.3847/0067-0049/222/1/8)
- Drout, M. R., Massey, P., Meynet, G., Tokarz, S., & Caldwell, N. 2009, *ApJ*, 703, 441, doi: [10.1088/0004-637X/703/1/441](https://doi.org/10.1088/0004-637X/703/1/441)
- Eggleton, P. P., & Cannon, R. C. 1991, *ApJ*, 383, 757, doi: [10.1086/170833](https://doi.org/10.1086/170833)
- Faulkner, J. 2005, in *The Scientific Legacy of Fred Hoyle*, ed. D. Gough, 149–226
- Gaia Collaboration. 2018, *A&A*, 616, A1, doi: [10.1051/0004-6361/201833051](https://doi.org/10.1051/0004-6361/201833051)
- Hoyle, F. 1960, *MNRAS*, 120, 22, doi: [10.1093/mnras/120.1.22](https://doi.org/10.1093/mnras/120.1.22)
- Iben, Icko, J. 1993, *ApJ*, 415, 767, doi: [10.1086/173200](https://doi.org/10.1086/173200)
- Imara, N., & Blitz, L. 2007, *ApJ*, 662, 969, doi: [10.1086/517911](https://doi.org/10.1086/517911)
- J Jeans, J. H. 1902, *Philosophical Transactions of the Royal Society of London Series A*, 199, 1, doi: [10.1098/rsta.1902.0012](https://doi.org/10.1098/rsta.1902.0012)
- Jermyn, A. S., Bauer, E. B., Schwab, J., et al. 2023, *ApJS*, 265, 15, doi: [10.3847/1538-4365/acae8d](https://doi.org/10.3847/1538-4365/acae8d)
- Kippenhahn, R., Weigert, A., & Weiss, A. 2013, *Stellar Structure and Evolution*, doi: [10.1007/978-3-642-30304-3](https://doi.org/10.1007/978-3-642-30304-3)
- Maeder, A. 2009, *Physics, Formation and Evolution of Rotating Stars*, doi: [10.1007/978-3-540-76949-1](https://doi.org/10.1007/978-3-540-76949-1)
- Miller Bertolami, M. M. 2022, *ApJ*, 941, 149, doi: [10.3847/1538-4357/ac98c1](https://doi.org/10.3847/1538-4357/ac98c1)
- Neugent, K. F., Massey, P., Skiff, B., & Meynet, G. 2012, *ApJ*, 749, 177, doi: [10.1088/0004-637X/749/2/177](https://doi.org/10.1088/0004-637X/749/2/177)
- Ou, P.-S., Chen, K.-J., Chu, Y.-H., & Tsai, S.-H. 2023, *ApJ*, 944, 34, doi: [10.3847/1538-4357/aca96e](https://doi.org/10.3847/1538-4357/aca96e)
- Paxton, B., Bildsten, L., Dotter, A., et al. 2011, *ApJS*, 192, 3, doi: [10.1088/0067-0049/192/1/3](https://doi.org/10.1088/0067-0049/192/1/3)
- Paxton, B., Cantiello, M., Arras, P., et al. 2013, *ApJS*, 208, 4, doi: [10.1088/0067-0049/208/1/4](https://doi.org/10.1088/0067-0049/208/1/4)
- Paxton, B., Marchant, P., Schwab, J., et al. 2015, *ApJS*, 220, 15, doi: [10.1088/0067-0049/220/1/15](https://doi.org/10.1088/0067-0049/220/1/15)
- Paxton, B., Schwab, J., Bauer, E. B., et al. 2018, *ApJS*, 234, 34, doi: [10.3847/1538-4365/aaa5a8](https://doi.org/10.3847/1538-4365/aaa5a8)
- Paxton, B., Smolec, R., Schwab, J., et al. 2019, *ApJS*, 243, 10, doi: [10.3847/1538-4365/ab2241](https://doi.org/10.3847/1538-4365/ab2241)
- Renzini, A. 2023, *MNRAS*, 521, 524, doi: [10.1093/mnras/stad159](https://doi.org/10.1093/mnras/stad159)
- Renzini, A., Greggio, L., Ritossa, C., & Ferrario, L. 1992, *ApJ*, 400, 280, doi: [10.1086/171995](https://doi.org/10.1086/171995)
- Renzini, A., & Ritossa, C. 1994, *ApJ*, 433, 293, doi: [10.1086/174645](https://doi.org/10.1086/174645)
- Ritossa, C. 1996, *MNRAS*, 281, 970, doi: [10.1093/mnras/281.3.970](https://doi.org/10.1093/mnras/281.3.970)
- Schmidt, E. G. 1984, *ApJ*, 287, 261, doi: [10.1086/162685](https://doi.org/10.1086/162685)
- Schönberg, M., & Chandrasekhar, S. 1942, *ApJ*, 96, 161, doi: [10.1086/144444](https://doi.org/10.1086/144444)
- Sugimoto, D., & Fujimoto, M. Y. 2000, *ApJ*, 538, 837, doi: [10.1086/309150](https://doi.org/10.1086/309150)
- Whitworth, A. P. 1989, *MNRAS*, 236, 505, doi: [10.1093/mnras/236.3.505](https://doi.org/10.1093/mnras/236.3.505)
- Yang, M., Bonanos, A. Z., Jiang, B.-W., et al. 2019, *A&A*, 629, A91, doi: [10.1051/0004-6361/201935916](https://doi.org/10.1051/0004-6361/201935916)
- Yang, M., Bonanos, A. Z., Jiang, B., et al. 2021, *A&A*, 646, A141, doi: [10.1051/0004-6361/202039475](https://doi.org/10.1051/0004-6361/202039475)
- Zaritsky, D., Harris, J., Thompson, I. B., & Grebel, E. K. 2004, *AJ*, 128, 1606, doi: [10.1086/423910](https://doi.org/10.1086/423910)